$CdSe/MoS_2$ interfaces designed as gigahertz/terahertz electro-optical filters

A. F. QASRAWI[1,2,*], W. S. GHANNAM[1]
[1]*Department of Physics, Arab American University, Jenin, Palestine*
[2]*Department of Electrical and Electronics Engineering, Istinye University, 34010, Istanbul, Turkey*

CdSe thin films coated with MoS_2 nanosheets were deposited by thermal evaporation to act as electro-optical filters in gigahertz/terahertz domains. Structural studies showed amorphous MoS_2 growth on polycrystalline CdSe. MoS_2 coating increased defects, microstrain, and reduced CdSe band gap from 2.09 eV to 1.95 eV, enhancing dielectric quality factor to several hundreds. Optical conductivity revealed cutoff frequencies from 0.06–5.66 THz within 1.15–3.50 eV. Signal propagation exhibited drift mobility of~52 cm^2/Vs and carrier density of~10^{16} cm^{-3}. Electrical tests showed microwave resonators, negative capacitance, and cutoff up to 350 GHz at 1800 MHz, enabling 6G applications.

(Received September 18, 2025; accepted June 2, 2026)

Keywords: $CdSe/MoS_2$, Electro-optic, Negative capacitance, Terahertz, Microwave

1. Introduction

CdSe in thin film form captured the interest of researchers because of their important applications in electro-optical systems. CdSe thin films are used as substrates suitable for many heterojunction devices. As for examples, CdSe/ZnTe solar cells exhibited external quantum efficiency of ~60% in the visible range of light [1]. These solar cells displayed an open circuit voltage of 0.33 V [1]. $CdSe/Bi_2Se_3$ heterojunctions are also utilized as wavelengths dependent bipolar photodetectors showing responsivity of 0.30-33.3 mA/W when exposed to light of wavelengths in the range of 405-830 nm [2]. CdSe thin films were also employed as photocatalytic materials for degradation of toxic dyes and as thermoelectric material [3]. In addition, oxide coated CdSe thin films were reported as a promising heterojunction for thin film transistor technology. One of these devices is $Au/CdSe/GeO_2/C$ metal oxide semiconductor field effect transistors (MOSFET) [4]. These MOSFETS were found suitable for the fabrication of microwave cavities [4].

Reports that considered the applications of CdSe thin films in terahertz technology as electro-optical filters are relatively rare. The aim of this work is to adapt CdSe films as electro-optical filters utilizable in terahertz technology. However, because CdSe suffers from lack of conductivity control and instability under ambient conditions prohibiting large scale of applications [5]. The motivation of the current work was induced by enhancing the features of CdSe films so that they suit electro-optical applications as stable optical filters. For this purpose, here in this work, CdSe films are coated with transparent MoS_2 layer of thickness of 100 nm to isolate it from air to avoid surface oxidation [6]. However, as MoS_2 nanosheets are known for their stability of semiconductor characteristics over very large areas they can serve as a protecting layer for CdSe without much altering of their properties [7]. Works which are concerned with the $CdSe/MoS_2$ interface mentioned that $CdSe/MoS_2$ hetero-structures with the ultra-large coverage of CdSe on MoS_2 guarantee efficient charge transfer across the hetero-interface [7]. Such interface was employed as photodetectors displaying current responsivity of 12 A/W and fast photoresponse of 370 μs [7].

Studies concerned with interfacial interaction between CdSe and MoS_2 mentioned their ability for neuromorphic applications [8]. In addition to their ability to perform as smart solar cells [9]. Like other Se and Cd based materials (CdTe, InSe, GaSe, SnSe), the excellent performance of such devices resulted from the nonlinear optical properties [10-12]. The nonlinear responses (for example, intensity-dependent absorption and refractive index) facilitate ultrafast light-controllable modulation of carrier generation and transport at the interface, which is fundamental for photonic synaptic functions in neuromorphic systems. In addition, the nonlinear responses significantly enhance light-matter interaction and optical gain for photoresponse, switching sensitivity, and efficiency in smart solar cell configurations [14,15].

The work here is concerned with using $CdSe/MoS_2$ heterojunction as electro-optical filters adequate for gigahertz/ terahertz technology applications. Initial stages of the current work will focus on the basic structural and optical properties of the heterojunction devices then a special focus on the dielectric properties, optical conductivity and terahertz cutoff frequency will be given. The heterojunction devices will be subjected to signals of low amplitudes to explore their responses in the gigahertz frequency domain.

2. Experimental details

High purity Cadmium selenide crystal lumps (99.999% metal basis from Alfa Aesar) are used as a source material to produce CdSe thin films. The CdSe films are grown onto cleaned glass substrates using a 0.35 g of CdSe grains situated in a tungsten boat specialized for CdSe. A film of thickness of 750 nm was produced by evaporating the CdSe

grains using the vacuum deposition method in a NORM VCM-600 evaporator. The vacuum level was fixed at 10^{-5} mbar prior to evaporation. The 750 nm thickness was preferred to achieve uniform and well adhered films. The film thickness was monitored via an INFICON STM-2 thickness monitor attached to a quartz crystal positioned in the evaporation chamber. The thickness monitor is qualified to register 3000 reading per second. The device resolution is 0.037 Å. CdSe thin films were prepared at an evaporation rate of 10 Å/s. Cleaned glass and some of the fabricated CdSe films are used as a substrate to deposit thin layers of Molybdenum di-Sulfide to form CdSe/MoS_2 heterojunctions. The source material for the evaporation of MoS_2 was 98%pure powders (Alfa Aesar). The coating of a 100 nm thick MoS_2 layer was produced in two sequential stages. At each stage an MoS_2 film of thickness of 50 nm was produced. This procedure was followed because the evaporation rate of MoS_2 is very low (2 Å /s) and long-term evaporation may result in over heating of the substrate as the target was to produce films at substrate temperature of 300 K. Because MoS_2 powders are very tiny and spreads out of the resistive heating boat like resistor. The MoS_2 powders were initially pressured at 200 bars in pellet form. The morphological, structural and optical data were collected with the assistance of COXEM-200 scanning electron microscope, X-ray diffraction unit (Rigaku Miniflex 600 unit) and Evolution 350 spectrophotometer, respectively. The spectrophotometer has a PIKE VEE MAX II variable angle reflectometer installed in its compartment. Impedance spectroscopy measurements were handled using Agilent 4291B 0.001–1.80 GHz impedance analyzer. The hot probe technique was used to determine the conductivity type of the films, which revealed n-type conductivity for both films.

3. Results and discussion

The optical images and the schematics for the proposed CdSe/MoS_2 heterojunctions are shown as inset-1 in Fig. 1. As seen from the inset, while CdSe films is brown colored, MoS_2 nanosheets are colorless. Depositing MoS_2 onto CdSe makes the brown color darker. Fig. 1 also display the X-ray diffraction (XRD) patterns for CdSe, MoS_2 and CdSe/MoS_2 films. It is evident from the figure that the XRD of CdSe film displayed 5 peaks located at 2θ values of 23.20°, 25.60°, 42.20°, 49.75° and 58.85°. The most intensive peak is observed at diffraction angle of $2\theta = 25.60^\circ$. Deep analyses of the X-ray diffraction patterns in accordance with "crystdiff" software packages indicated that the first, second and fourth peaks are assigned to hexagonal CdSe. The estimated lattice parameters in accordance with the observed reflection peak are found to be $a = b = 4.43$ Å and $c = 6.96$ Å. The hexagonal cell parameters of CdSe are close to those listed in cards of open crystallography data base (COD: 9016056) as 4.299 and 7.01 Å along the $a-$ and $c-$axis, respectively, with space group of P63mc. The lattice parameters of the hexagonal CdSe films reported here are consistent with literature data where a value of $a = b = 4.250$ Å and $c = 7.092$ Å were reported [15]. The XRD peaks observed at diffraction angles of $2\theta = 42.20^\circ$ and 58.85° are assigned to the cubic structure of CdSe. The calculated lattice parameters of the cubic cell are found to be $a = b = c = 6.05$ Å consistent with the value reported as $a = 6.077$ Å and as $a = 6.08$ Å for the cubic CdSe [16].

As also observed in the XRD patterns presented in Fig. 1, no intensive peaks are observed in the XRD patterns of MoS_2 films, indicating the amorphous nature of grown nanosheets. Such structure probably resulted from the formation of polymorphic phases. Since MoS_2 is known to exhibit monoclinic, orthorhombic, hexagonal, cubic, trigonal and tetragonal structures [17]. The presence of these phases together in the same film forces the MoS_2 to exhibit amorphous structure. On the other hand, glass transition and random orientation of small grains and nanoclusters accompanied with large grain boundaries may also be regarded as a reason for the formation of the amorphous phase of the MoS_2 film [18].

As observed in inset-2 of Fig. 1, the positions of the strongest two peaks are shifted from 23.20° and 25.60° to 23.35° and 25.80°, respectively. Moreover, the minor peak which is located at diffraction angle of $2\theta = 58.85^\circ$, that represents the cubic phase of the CdSe films in the (014) direction, disappeared upon interfacing the CdSe with MoS_2. The other diffraction pattern which is assigned to the cubic structure appeared at diffraction angle of 42.60^o.The large shift ($\Delta 2\theta = 0.40°$) in the position of this peak indicates that a deformation process is associated with materials interfacing. In addition, the peak which represents a minor phase that was assigned to Cubic CdSe being indexed in the (111) direction is also observed in the CdSe/MoS_2 at 2θ of 49.75°. The calculated values of the phase weight ($\Delta\%=100\frac{\sum A_{Hex}}{\sum A_{all\ peaks}}$; area of the peak) of the reflection peaks in accordance with "measure" software packages revealed a value of 79% and 21% for hexagonal CdSe and cubic CdSe, respectively. It is obvious from inset-2 of Fig. 1 that, the depositions of MoS_2 onto the CdSe films lead to a remarkable decrease in the XRD intensity of the maximum peak. Namely, the intensity decreases from 5.48×10^3 to 4.31×10^3 Counts/s, the peak is broadened and peak position is shifted from $2\theta = 25.60^\circ$ shifts to $2\theta = 25.80^\circ$ This means that the maximum peak becomes broadened indicating the plastic deformation process in the films [19]. The analysis of the reflection peaks for the hexagonal CdSe/MoS_2 heterojunctions indicated a decrease in the lattice constants along the a and c -axes as a result of coating the MoS_2 layers onto CdSe. The XRD analyses revealed a value of 4.40 Å and 6.90 Å for the a and c, respectively, for the hexagonal phase and a value of 6.00 Å for the cubic phase.

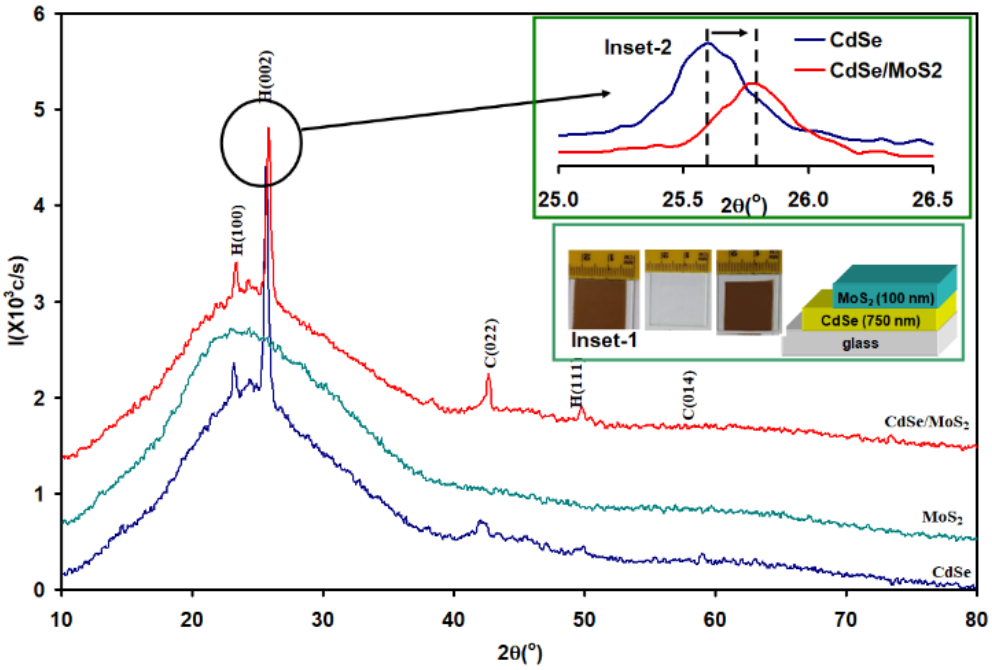

Fig. 1. XRD patterns for films of CdSe, MoS_2 and CdSe/MoS_2 heterojunction devices. Inset.1showing the optical images and schemastics of the samples. Inset. 2 showing the shift in the XRD main peak (colour online)

On the other hand, the calculated crystallite size $D = 0.94\lambda/(\beta\cos(\theta)$, the strain $\epsilon = \frac{\beta}{4\,tan\theta}$, the stacking faults percentages $SF\% = \frac{2\pi^2\beta}{45\sqrt{3\tan(\theta)}}$, and the defect density along the a and $c-$axis $\delta = \frac{15\,\varepsilon}{a\,D}$ [4] are listed in Table-1. Here β is the maximum peak broadening calculated at full wave half maximum. As seen from the table, the presence of MoS_2 causes an increase in the strain, stacking faults and defect density along both of the a and $c-$axis. The crystallite size also decreased to 28 nm. Particularly, the decrease in the crystallite sizes relate to the fact that there is an enormous number of bonding. It is possible for one bonded atom to leave its site creating defects [20]. Conversely, each atom in a broken bond may be attracting another atom in another bond. Such interaction forces usually lead to the strained structure leading the crystallite size of CdSe to be reduced upon the CdSe/MoS_2 interfacing. The grain boundaries are altered as a result of the change in the crystallite size which in turn alters the electrical conduction in the CdSe. Moreover, the increased dislocation density caused the energy to be stored in the grains, leading sub grains and enlargement or shrink in the existing grains. Such a process increases the trap states that act as recombination centers in the materials [21].

Table 1. The structural parameteres of the main peak of CdSe and CdSe/MoS_2 heterojunction device

Sample	2θ (°)	I (X10^3 c/s)	Miller indices			Lattice constant (Å)		D (nm)	$\epsilon \times 10^{-3}$	SF%	δ(X10^{12}line/cm^2)	
			h	k	l	a-axis	c-axis				a-axis	c-axis
CdSe	25.60	5.48	0	0	2	4.43	6.96	34	4.80	0.23	4.78	3.04
CdSe/MoS_2	25.80	4.31	0	0	2	4.40	6.90	28	5.72	0.28	6.87	4.37

For further explanation of the changes in the structural parameters, it is possible to think that, at the surface there should be non-interacting Mo and S atoms exhibiting ionic radius of 0.65 Å and is 1.84 Å [22] which are, respectively, much lower than that of Cd 0.97 Å and Se (1.98 Å) [23]. As CdSe can exhibit Cd or Se vacancies [24], probably, Mo and S ions, respectively, replaces vacant sites of cadmium forming Mo-Se and Cd-S bonds.

Fig. 2 (a) and (b) show the scanning electron microscopy images (SEM) for CdSe and CdSe/MoS_2 films, respectively. As seen from Fig. 2 (a) CdSe grows in cloud shaped clusters mostly of amorphous appearance. The clusters contained randomly distributed grains. Enlargement of this region by 20000 times (inset of Fig. 2 (a)) showed that the grains are either rectangular or oval shaped. The average size of these grains is 230 nm. As seen from Fig. 2 (b) coating CdSe films with MOS_2 resulted in the disappearance of these large grains and very homogeneous surface appears probably due to the amorphous nature of MoS_2. The rarely observed large grains appearing on the surface of MOS_2 layer are probably related to uncovered CdSe grains. The average size of the grains remaining on the surface of MoS_2 are 200 nm. In accordance with these numerical data, the grain size of CdSe decreased by 16.7%. This percentage is close to that (17.6%) obtained from the crystallite size calculations

(Table 1). Recalling that the grain is an accumulation of groups of crystallites then the reduction in the size of the grain is owed to the decreased crystallite size.

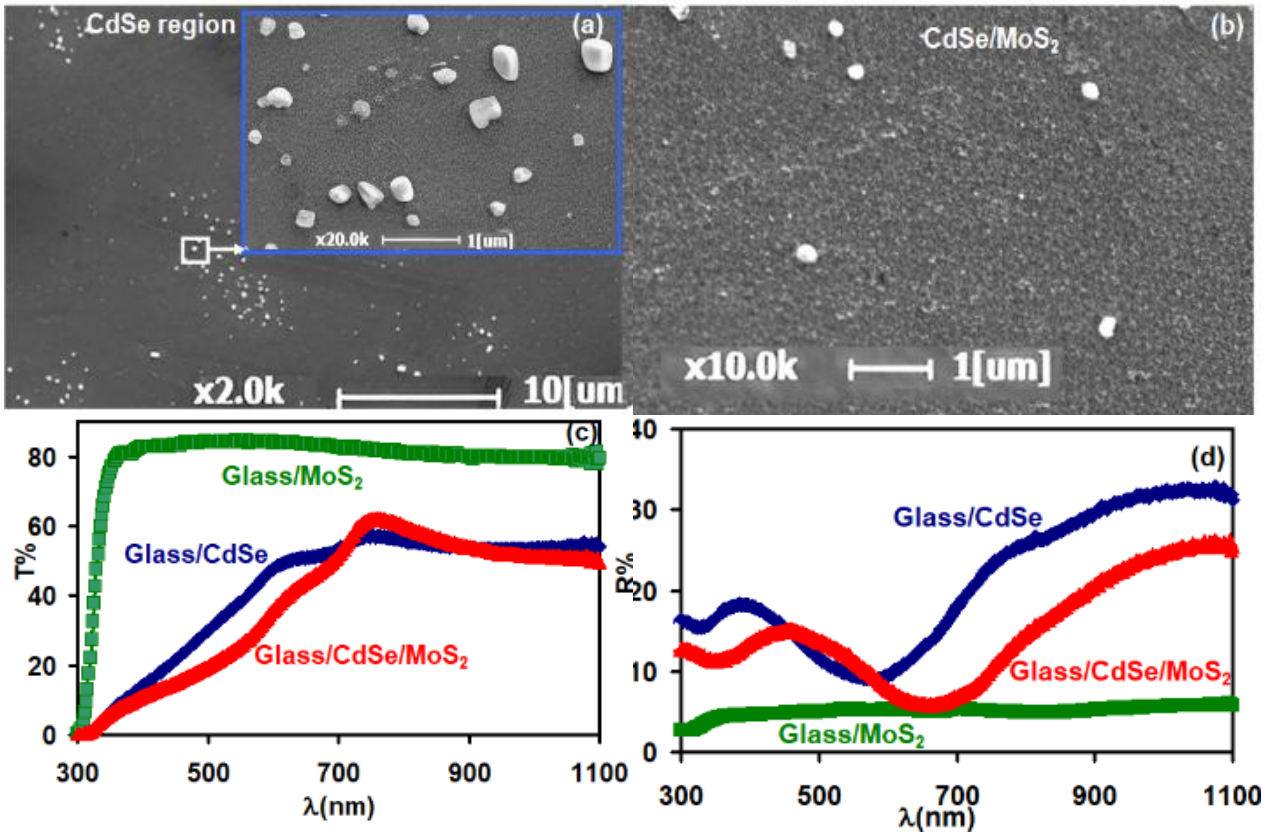

Fig. 2. The scanning electron microscopy images for (a) CdSe films, (b) CdSe/ MoS_2 heterojunctions and the optical (c) transmittance and (d) reflectance for CdSe, MoS_2 and CdSe/MoS_2 heterojunction devices.Inset of (a) showing an enlargement by 20 k times of a small region collected from CdSe films (colour online)

The role of the Molybdenum disulfide layers on the optical properties of CdSe thin films are investigated by means of visible light spectrophotometry technique. The transmittance (T) and reflectance (R) spectra were measured in the wavelength (λ) region of 300–1100 nm. The measured T and R spectra for CdSe, MoS_2 and CdSe/MoS_2 heterojunctions are presented in Fig. 2 (c) and (d), respectively. As shown from the T spectra which are illustrated in Fig. 2 (c), MoS_2 films are highly transparent compared to CdSe. The spectra show a shoulder at 370 nm. The value of T spectra increased with increasing λ until λ= 400 nm is reached. For all λ>400 nm, T of MoS_2 has tendencies of decreasing. For the CdSe films, the transmittance spectra exhibit a shoulder and one main peak positioned at 642 nm (1.94 eV) and 750 nm (1.66 eV), respectively. The T spectra of CdSe coated with MoS_2 indicated that the effect of deposition of MoS_2 layers on the CdSe film become effective when incident light wavelengths is larger than 380 nm. It is clear from the figure that, the major peak become more pronounced and exhibit higher T values associated with redshift in the observed peak. The peak shifts from 750 nm (1.66 eV) to 766 nm (1.62 eV). Similarly, R spectra which are evident in Fig. 2 (d) displayed decreasing R values accompanied with a redshift in the observed peaks position. Particularly, the peaks of maximum reflectance shift from 302 nm (4.11 eV), 400 nm (3.11 eV) and 1086 nm (1.14 eV) in the reflectance spectra of CdSe to 306 nm (4.06 eV), 466 nm (2.67 eV) and 1092 nm (1.14 eV) upon adding the MoS_2 layer.

In addition, the absorption coefficient (α) spectra for CdSe, MoS_2 and CdSe/MoS_2 heterojunction which are obtained from the measured transmittance and reflectance spectra with the help of equation, $\alpha = -d^{-1}\ln\left(\frac{T}{(1-R_{glass})(1-R_{CdSe})(1-R_{CdSe/MoS2})}\right)$ are shown in Fig. 3 (a) for MoS_2 and Fig. 3 (b) for CdSe and CdSe/MOS_2 films. The α −spectra of MoS_2 films show a different behavior from CdSe and CdSe/MoS_2. Its absorption coefficient decreases with decreasing incident photon energy (E) until reaching 2.00 eV. In the region below 2.00 eV, the α − spectra of MoS_2 exhibit increasing trends of variation with decreasing incident light energy (inset of Fig. 3 (a)). This behavior is assigned to the free carrier absorption that arises from the presence of free electrons, lattice distortion and carrier transitions within conduction band [25]. In addition, as seen from the inset of Fig. 3 (a), in the low absorption region, α −spectra of CdSe and CdSe/MoS_2 decreases following a smoother trend of

variation. This behavior is probably assigned to the existence of extended band tails in the band gap of CdSe and CdSe/MoS_2. Actually, the fitting of the Urbach rule ($\alpha = \alpha_o e^{E/E_u}$; α_o is pre-exponential factor [25]) which is shown in Fig. 3 (c) displayed linear trends of variations s that permit calculation of the Urbach tails width (E_u) as 0.90 eV in the band structure of CdSe and as 0.27 eV for CdSe/MoS_2 interfaces. Energy bad tails can result from the orbital overlapping between energy levels and from the presence of large number of defects, vacancy, impurities, broken bonds and inhomogeneities [25]. Because the electronic configuration of Cd, Mo, Se and S are $4d^{10}5s^2$, $4d^5\ 5s^1$, $3d^{10}\ 4s^2\ 4p^4$ and $3s^2\ 3p^4$, respectively, 4d orbitals of Mo ions overlaps with 4d orbitals of Cd atoms. Moreover, the coating of MoS_2 onto CdS decreased the width of the band tails due to the filling of vacant sites of Cd and Se in CdSe as mentioned previously in XRD analysis.

From the other point of view, as shown in Fig. 3 (d), the Tauc's equation ($(\alpha E)^2 \propto (E - E_g)$ [25]) fitting for direct allowed transitions revealed E −axis crossings of 2.09 eV and 1.95 eV and 1.95 eV for CdSe, MoS_2 and CdSe/MoS_2 films, respectively. CdSe is mentioned exhibiting three energy band gaps centered at 1.732 eV, 1.761 eV and 2.161 eV, respectively [25]. These band gaps originated from transitions between $\Gamma_{9v} - \Gamma_{7c}$, $\Gamma_{7v} - \Gamma_{7c}$ and $\Gamma_{7v} - \Gamma_{7c}$ of the first Brillouin zone of hexagonal CdSe, respectively [26]. The most popular value of E_g of CdSe is 1.74 eV.

However, values of band gap close 2.0 eV like 2.05 eV and 2.161 eV are assigned to the spin orbit splitting at Γ point which results in an energy band gap difference of 0.418 eV [25]. Hence the lowering of the energy band gap of CdSe to 1.95 eV (which is the band gap of MoS_2, recorded here) should be due to the further overlapping between orbitals of Cd, Mo, Se and S [25]. The optical energy band gap of MOS_2 being 1.95 eV is also close to that reported in literature as 1.971 eV [25]. Literature reports an optical band gap of 1.66 eV at room temperature for MoS2_22 thin films with a thickness of 600 nm, which is close to the bulk value and is lower than that typically observed for nanosheets (~100 nm or thinner) [27]. The difference between our measured band gap and the literature value can be attributed to the inverse dependence of band gap on film thickness [27]. A similar thickness dependence has been reported for CdSe: a band gap of 1.71 eV was measured for 1200 nm films deposited by thermal evaporation [28], whereas the CdSe films in this work are thinner (750 nm).

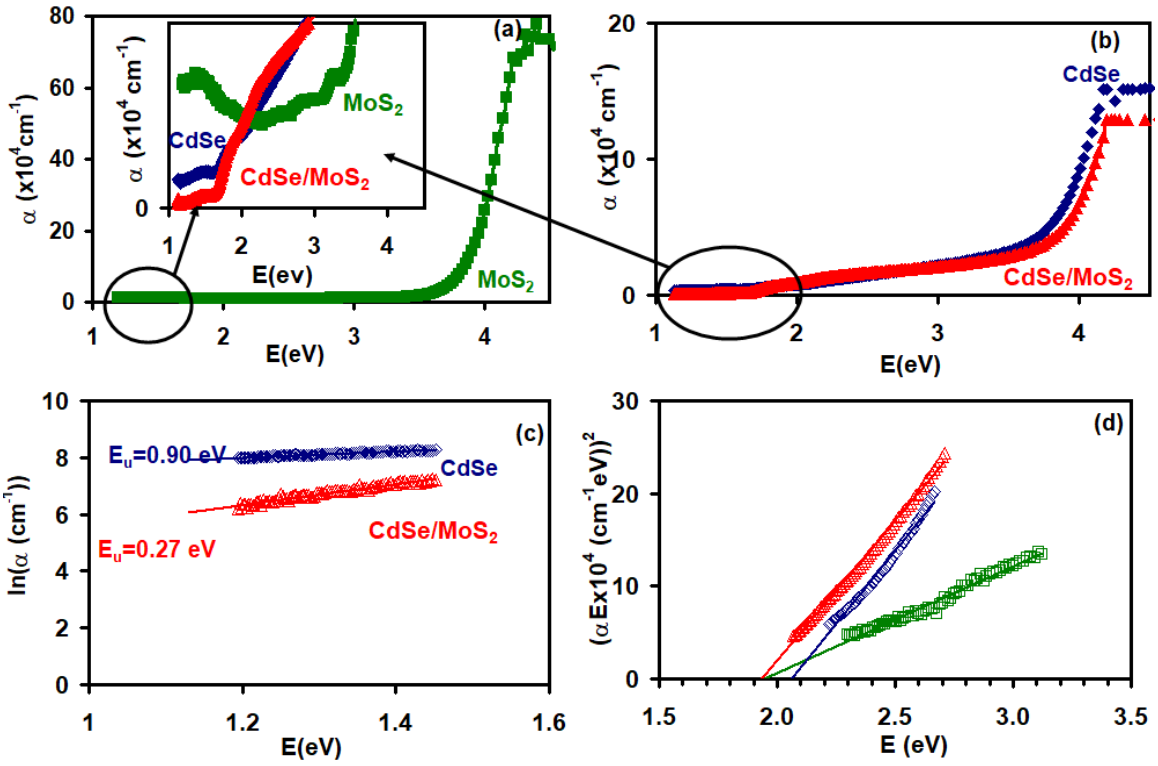

Fig. 3 The optical absorption coefficient spectra for (a) MoS_2, (b) CdSe and CdSe/MoS_2 films (c) The ln(α)-E variations and (d) the Tauc's equation fittiniungs for CdSe, MoS_2 and CdSe/MoS_2 heterojunction device (colour online)

To investigate possible applications of the CdSe/MoS_2 heterojunction, the real (ε_r) and imaginary (ε_{im}) parts of the relative dielectric spectra are estimated. ε_r and ε_{im} which are calculated using the relation [25],

$$\varepsilon_r = n(\omega)^2 - k(\omega)^2 \quad (1)$$

$$\varepsilon_{im}(\omega) = 2n(\omega)k(\omega) \quad (2)$$

$$n(\omega)=\frac{1+R(\omega)}{1-R(\omega)}+\sqrt{\frac{4R(\omega)}{(1-R(\omega))^2}-k(\omega)^2}, k(\omega)=\frac{c\alpha}{\omega} \quad (3)$$

here, $n(\omega)$ and $k(\omega)$ are the refractive index and the extinction coefficient, respectively. $\omega = E/\hbar$ is the angular frequency of the propagating light signal. ε_r spectra for the CdSe, MoS_2 and CdSe/MoS_2 films are illustrated in Fig. 4 (a). The inset of Fig. 4 (a) which is an enlargement of dielectric constant spectra for MoS_2 films show that in the spectral range of 3.36-4.0 eV, the dielectric constant of amorphous MoS_2 film sharply increases with decreasing incident photon energy. It then approaches a constant value in the spectral range of 1.60-3.35 eV. In the spectral range of 1.13-1.35 eV, the dielectric constant increases again. As it is also evident from Fig. 4 (a), the real part of the dielectric spectra of CdSe exhibit two peaks centered at 1.17 eV and 3.15 eV. Although the dielectric spectra of CdSe coated with MoS_2 display the same behavior like that of CdSe, there are a redshift in the minor peak accompanied with a decrease in the value of the real part of dielectric constant. Particularly, ε_r spectra for CdSe exhibit a resonance peak of ε_r value of 6.20 at critical energy of 3.15 eV. Coating MoS_2 shifted the resonance peaks to 2.67 eV and decreased the value of the dielectric constant to 5.14. The resonant peak at 3.15 eV in the CdSe film is attributed to electronic transitions from the valence band's Se 4p states to the conduction band's Γ_{3c} point in the first Brillouin zone of selenium [29]. The appearance of the resonance peak in the real dielectric spectra of CdSe/MoS_2 at 2.67 eV is probably due to the transition between Cd and S from the valence band (Γ_{5v}) to the conduction band (Γ_{1c}) as it is very close to this energy band gap of CdS 2.79 eV [29]. The redshift in the dielectric constant spectra may be assigned to the increase in the defect density of CdSe due to MoS_2 stacking. The increased defect density leads to change in the recombination mechanism. As we also see from the figure, both CdSe and CdSe/MoS_2 displayed the same maximum peak position of ε_r which appear at 1.17 eV with ε_r values being decreased from 13.20 to 9.26 due to the coating of CdSe with MoS_2 nanosheets. Moreover, the dielectric constant spectra of CdSe/MoS_2 heterojunction showed a slight decrease of the high frequency dielectric constant (ε_∞) value from 5.46 for single layer CdSe to 4.46 for double layer. The ε_∞ value is close to that reported for CdSe as 6.20 [29], [30].

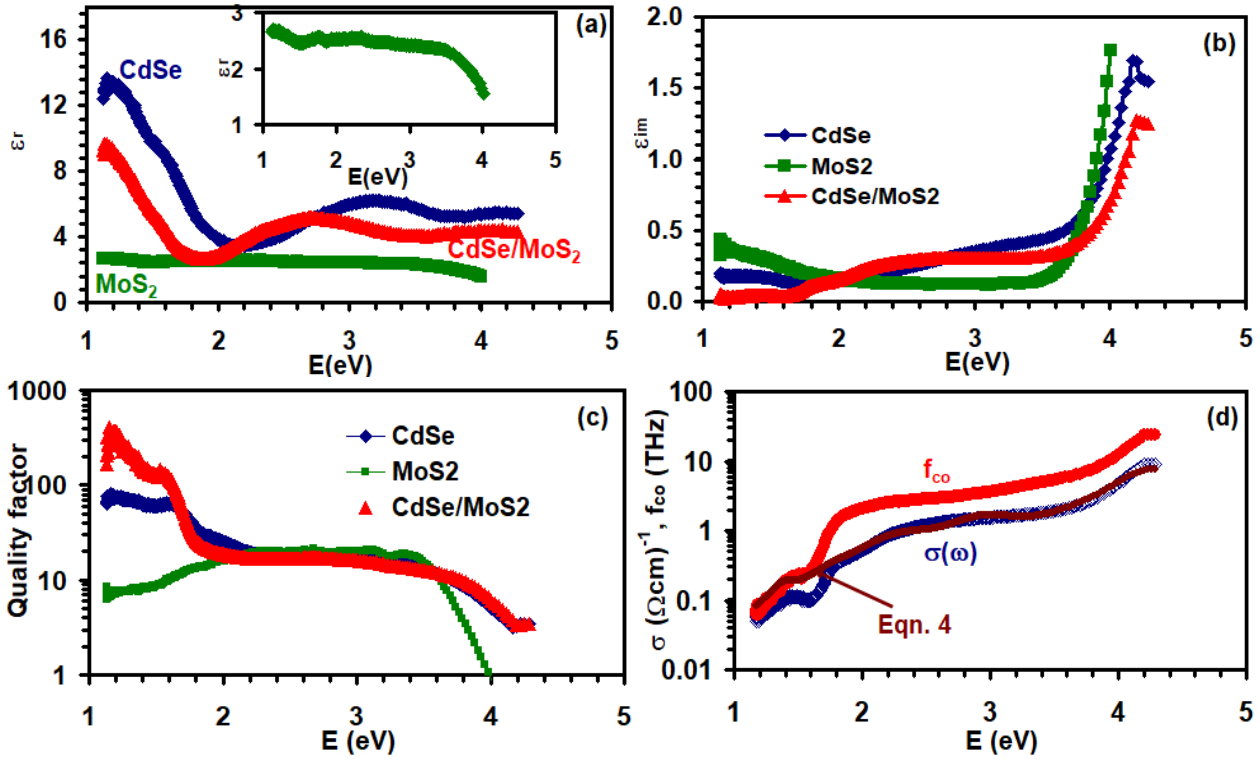

Fig. 4. (a) The real part and (b) the imaginary part of the dielectric spectra and (c) the quality factor spectra for CdSe, MoS_2 and CdSe/MoS_2 heterojunction. (d) showing the optical conductivity and cutoff frequency spectra for the CdSe/MoS_2 enhanced dielectric layer. Inset of (a) represent an enlargement of the dielectric constant spectra of MoS_2 films (colour online)

The analysis of the imaginary part of the dielectric constant spectrum serves as a crucial link between optical and electrical properties, as it is directly related to optical conductivity. ($\sigma(w) = (\varepsilon_{im} w/4\pi)$; w is the angular frequency). The ε_{im} spectra for the CdSe, MoS_2 and CdSe/MoS_2 heterojunctions are presented in Fig. 4 (b). In accordance with this figure, the ε_{im} displays significantly low values compared to the real part. The ε_{im} spectra of CdSe exhibit steady behavior and reveal a value of 0.19 in the spectral range of 1.10 eV-1.60 eV. It then, increases with increasing photon energy in the high energy range exhibiting a value 1.69 at 4.16 eV. The same trends of

variation are also observed in the ε_{im} spectra of CdSe/MoS_2 with smaller values of ε_{im}. One important feature of the ε_{im} spectra of the CdSe coated with MoS_2 is that; the ε_{im} increases until reaching 2.70 eV and remains constant in the energy range of 2.70-3.50 eV. On the other hand, the ε_{im} for MoS_2 represents a different behavior than that of CdSe and CdSe/MoS_2. It's clear from the figure that, the imaginary part of the dielectric constant of MoS_2 decreased from 0.39 to 0.14 at energy values 1.10 eV and 3.50 eV, respectively. For E>3.50 eV, the ε_{im} of MoS_2 highly increases exhibiting a value of 1.77 at 4.00 eV.

For a dielectric layer suitable for storing electromagnetic energy, the quality factor ($Q = \varepsilon_r/\varepsilon_{im}$) provides information about the sensitivity of the dielectric layer [31]. The quality factor spectra for CdSe, MoS_2 and CdSe/MoS_2 are illustrated in Fig. 4 (c). The figure shows the low-quality factor for MoS_2 layers as compared to those of CdSe and CdSe/MoS_2. Coating CdSe with MoS_2 increased the quality factor significantly. Pronounced Q values become visible as the light energy decreased below 1.75 eV. Values of Q exceeding 400 are reached at 1.15 eV for CdSe/MoS_2 electro-optical layers. It means that depositing of MoS_2 nanosheets onto CdSe highly improved the dielectric response of CdSe.

For the enhanced CdSe/MoS_2 dielectric layer, the optical conductivity and the terahertz cutoff frequency ($f_{co} = \frac{\sigma(\omega)}{\varepsilon_r(\omega)}$) spectra are illustrated in Fig. 4 (d). Both of the conductivity and the terahertz cutoff frequency spectra show the same trends of variation. The cutoff frequency exhibited values in the range of 0.060 -1.67 THz as the light signal frequency increased from 1.15 eV to 1.86 eV. This range of light corresponds to the IR range which has many applications in terahertz technology. Like 6G technology and IR imaging [32,33]. Increasing the light signal further, slightly altered the optical conductivity and terahertz cutoff frequency values. Namely, the cutoff frequency increased from 1.70-5.66 THz as the light energy increased from 1.90 eV to 3.50 eV, respectively. Tendency of light to reach ultraviolet range forced sharper increase in the cutoff frequency values. Values of cutoff frequency reaching 25 THz are reported for ultraviolet communication systems adapted for 5G technology [34]. More specific information about the electro-optical parameters of the enhanced CdSe/MoS_2 dielectric layer is gained from the modeling on the optical conductivity using Drude-Lorentz approach for optical conductivity-frequency dependence [25]. The optical conductivity is given by the relation [25],

$$\sigma(\omega) = \sum_{i=1}^{N} \frac{p_i e^2}{4\pi\varepsilon_o m^*} \frac{\gamma_i \omega^2}{\left((\omega_{ei}^2 - \omega^2)^2 + (\gamma_i \omega)^2\right)}, \quad \gamma = \tau^{-1} \tag{4}$$

In this equation, $\omega_{ei} = E_{ei}/\hbar$ is the electron-plasmon reduced frequency whose energy is E_{ei}. The reduced mass is $m^*_{CdSe/MoS_2} = ((m^*_{CdSe})^{-1} + (m^*_{MoS_2})^{-1})^{-1} = 0.102\, m_0$ [34,35]. τ is the average scattering time and represents the inverse of the damping coefficient (γ). The free-electron drift mobility is also determined by the formula $\mu = e\tau/m^*$. The experimental data of optical conductivity was reproduced by fitting Eqn. 4 through inserting the value of the effective masses as $0.102\, m_0$ [35] and $0.48\, m_0$ [34], for $n-$ CdSe and $n-$ MoS_2, respectively. Running the series in Eqn. 4 up to $k = 6$, allowed re-production of the experimental data. The estimated optical conductivity is presented by brown colored circles in Fig. 4 (d). The theoretically estimated optical conductivity parameters are listed in Table-2. As seen from the table two of the six excited oscillators are active in the infrared range of light ($E_{e1} = 1.38$ eV, $E_{e2} = 1.77$ eV), two are active in the visible range of light ($E_{e3} = 2.30$ eV, $E_{e4} = 1.77$ eV) and two are active in the ultraviolet range ($E_{e5} = 3.61$ eV, $E_{e6} = 4.27$ eV) of light. Except for the sixth oscillator, which exhibited low drift mobility and very high carrier concentration, all other oscillators are very adequate for the production of thin film transistors workable in terahertz frequency technology. The carrier concentration lay within the acceptable range (10^{16}-10^{18} cm^{-3}) of thin film transistors [35]. As the table also illustrates, the drift mobility values increased with decreasing oscillator energy. Higher mobility means faster charge carrier motion and lower power consumption [36]. Heterojunctions designed as bipolar transistors for sub-terahertz applications like millimeter-wave, imaging and sensing [37]. Literature data reported the design of high power, high frequency and terahertz wave electronics exhibiting mobility values of 50-1500 cm^2/Vs [38]. These systems with free carrier concentration in the range of 10^{12}-$10^{17}cm^{-3}$ are regarded as heterojunctions suitable as TeraFETs utilized in 6G technology [38].

It is interesting to compare the estimated optical conductivity parameters obtained here with other CdSe based heterojunction devices. MoO_3/CdSe heterojunction devices exhibited the highest drift mobility of 39.3 cm^2/Vs for infrared oscillator of energy of 1.38 eV [39]. The free carrier concentration is $1.5\times 10^{17} cm^{-3}$ [39]. CdSe/GeO also showed remarkable enhanced drift mobility values reaching 60 cm^2/Vs in the IR range of light [40]. The values obtained here are comparable with these previously determined indicating the compatibility of the proposed CdSe/MoS_2 system with those available in literature [39,40].

Table 2. The optical conductivity parameters for the CdSe/MoS_2 electro-optical terahertz band filters

$i =$	1	2	3	4	5	6
E_e (eV)	1.38	1.77	2.30	2.95	3.61	4.27
n (x10^{17} cm^{-3})	0.5	0.6	17.0	26.0	90.0	190.0
μ (cm^2/Vs)	51.71	34.48	13.79	15.51	13.79	0.53

Far from the optical analyses we attempted to construct a practical electronic component that performs as microwave band filters. The schematics of the experimental design are illustrated in the inset Fig. 5 (a). CdSe films were re-deposited onto commercial indium doped tin oxide (ITO) and then coated with MoS_2 layer of thickness of 100 nm and top contacted with Ag point contacts of areas of 3.14×10^{-2} cm^2. The ITO and Ag conducting electrodes was inserted between the terminals of an impedance analyzer generating signals in the freque3ncy rang of 10-1800 MHz. The imposed waveform signal was of low amplitude to allow detecting extremely weak signals. The measured resistance (R), capacitance (C) and impedance (Z) are shown in Fig. 5 (a). It can be seen from the figure that the impedance of the device is highly affected by the resistive part in the low frequency domain 10-1340 MHz. Significant difference between the impedance and resistance values becomes visible in the frequency domain of 1350-1800 MHz. In this domain the resistance sharply increases after exhibiting one local and one maximum peak. In general, the resistance decreases with increasing frequency due to the parasitic capacitive couplings [41] or due to the switching of the hoping electron transport [42].

Fig. 5 (a) also illustrates the capacitance spectra as function of low amplitude frequency. It is evident from the capacitance spectra that the capacitance exhibits resonance and anti-resonance phenomena at different position of the frequency axes. While positive peaks refereeing to resonance appear at critical frequencies of 127 MHz, 200 MHz and 820 MHz, antiresonance accompanied with negative capacitance appeared at frequencies of 100 MHz, 226 MHz and 796 MHz. The resonance anti-resonance phenomena which originated from resonance in the dielectric constant indicate the characteristics of microwave resonators [43]. Negative capacitance effect which dominates in all the spectral ranges except for the positive resonance positions is important for parasitic capacitance cancellation, noise reduction and signal amplification [43], [44]. This phenomenon was previously observed in CdSe/GaSe heterojunctions at 530 MHz, 1040 MHz and 140 MHz [45].

On the other hand, as a waveguide the gigahertz cutoff frequency ($f_{co} = 1/(2\pi RC)$) spectra is displayed in Fig. 5 (b). Remarkable enhancement in the gigahertz cutoff frequency is observed as the frequencies approaches the quad band frequency band defined at 1800 MHz. This quad band is globally used in Europe, Asia and Africa [46]. The cutoff frequency of the proposed CdSe/MoS_2 devices in this band reaches 350 GHz. The value here is ideal for 6G technology applications [46]. The result is also consistent with those obtained from optical measurements as the value here corresponds to 0.35 THz. Interesting feature of this value of the cutoff frequency lay in its coincidence with that reported as 340 GHz low noise amplifier chips designed from 01 mm wafer 35 nm InP high electron mobility transistors (HEMT) [47]. These transistors are nominated for terahertz communications, imaging and scientific instruments [47]. Other HEMT devices designed for radio astronomy applications and sensing exhibited cutoff frequency of 300 GHz which is also close to our foundation [48].

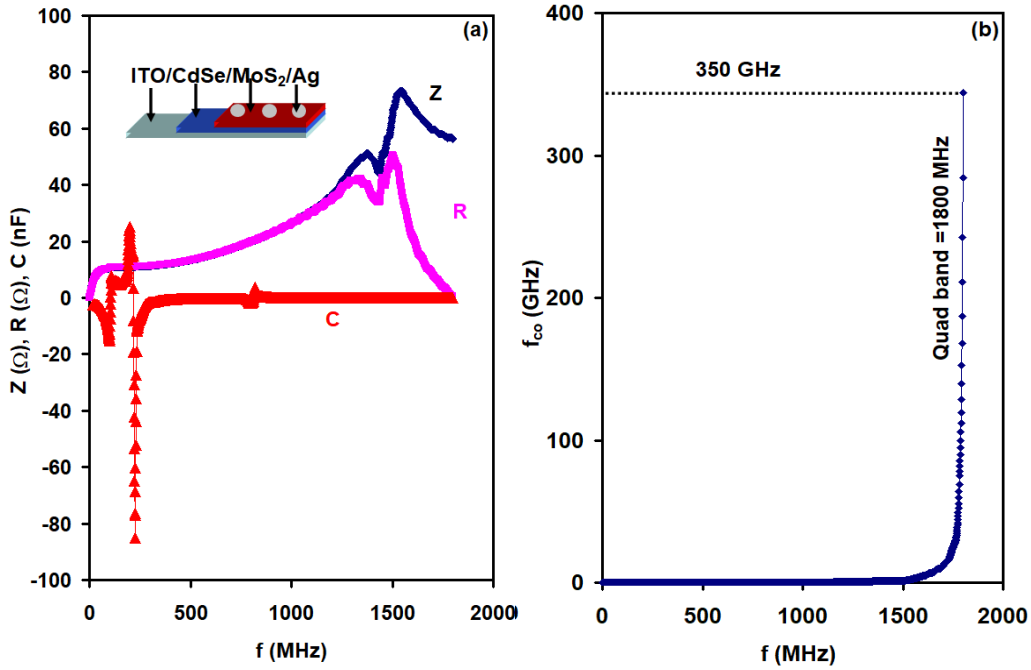

Fig. 5. (a) the resistance, cpacitance nad impedance and (b) the cutoff freqncy spectra for CdSe/MoS_2 electro-opitcla filters (colour online)

4. Conclusions

In the current work we have explored the effects of MoS_2 coating on the structural, optical, dielectric and electrical properties of CdSe designed as gigahertz/ terahertz band filters. The interfacing of CdSe/MoS_2 displayed structural properties of deformed amorphous/crystalline interfaces. The lattice constants along the a −and c −axes decreased from 4.43 Å and 6.96 Å to 4.40 Å and 6.90 Å, respectively. The respective increase in the defect concentrations reached 43.72% and 35.06%. Although the structure is deformed, the optical band gap is narrowed to 1.95 eV and shallow energy band tails of width of 0.26 eV is formed in the band gap of CdSe due to the MoS_2 coating. The coating of the epilayer on the CdSe decreased the dielectric constant values and enhanced the quality factor of the dielectric media up to 400. Numerically, the high frequency dielectric constant value decreased from 5. to 4.46 upon coating CdSe with MoS_2. In addition as a terahertz band filter workable in the incident photon energy range of 1.15-4.20 eV, CdSe/MoS_2 interfaces exhibited a terahertz cutoff frequency in the range of 0.06-5.66 GHz. The drift mobility of this system varied in the range of 0.53-51.71 cm^2/Vs based of the exciting photon energy with significant enhancement in the infrared range of light. Moreover, electrical investigations on the CdSe/MoS_2 devices showed their suitability as thin film transistors suitable for parasitic capacitance cancellation and signal amplification in addition to their features as waveguides workable in the gigahertz frequency domain and exhibiting a cutoff frequency up to 350 GHz. The study here proofed the suitability of the CdSe/MoS_2 system for high frequency applications as an electro-optical system.

Acknowledgements

This work was funded by the deanship of scientific research at Arab American University (AAUP), Jenin, Palestine and by Istinye University, Istanbul, Turkey. The authors therefore acknowledge the financial support of the AAUP and Istinye University.

References

[1] X. Bao, J. Xue, X. Yang, J. Liu, H. Yang, Z. Tang, J. Tang, C. Chen, X. Zeng, K. Li, Solar Energy Materials and Solar Cells **272**, 112878 (2024).
[2] W. Yan, F. He, M. Zhang, ACS Applied Materials and Interfaces **16** (32), 42461 (2024).
[3] S. T. Ahamed, C. Kulsi, D. Banerjee, D. N. Srivastava, A. Mondal, Surfaces and Interfaces **25**, 101149 (2021).
[4] N. M. Khusayfan, H. K. Khanfar, S. R. Alharbi, Materials Research **24** (5), e20210020 (2021).
[5] A. R. Wassel, S. A. Mansour, F. M. Mohamed, A. M. El-Mahalawy, Journal of Alloys and Compounds **976**, 173052 (2024).
[6] L. H. Qin, Y. Q. Yan, G. Yu, Z. Y. Zhang, T. Zhama, H. Sun, Materials **14** (15), 4097 (2021).
[7] Y. Yuan, X. Zhang, H. Liu, T. Yang, W. Zheng, B. Zheng, F. Jiang, L. H. Li, D. Li, X. L. Zhu, A. L. Pan, Journal of Alloys and Compounds **815**, 152309 (2020).
[8] X. Song, X. Lv, M. He, F. Mao, J. Bai, X. Qin, Y. Hu, Nanophotonics **13**, 4211 (2024).
[9] P. Pandey, Sh. Yadav, J. P. Pandey, R. K. Yadav, S. K. Ojha, B. Kumar, Journal of Optics (2024).
[10] M. Isik, N. Gasanly, Journal of Electronic Materials **54**, 9151 (2025).
[11] M. Isik, N. M. Gasanly, Applied Physics A **131**, 820 (2025).
[12] O. Surucu, G. Surucu, N. M. Gasanly, M. Parlak, M. Isik, Materials Letters **373,** 137078 (2024).
[13] B. Lamiya, A. Guseinov, F. Akhmedova, M. Isik, Micro and Nanostructures **213**, 208604 (2026).
[14] S. Delice, M. Isik, H. H. Gullu, M. Terlemezoglu, O. B. Surucu, M. Parlak, N. M. Gasanly. Journal of Physics and Chemistry of Solids **131**, 22 (2019).
[15] C. Narula, R. P. Chauhan, Radiation Physics and Chemistry **144**, 405 (2018).
[16] N. Garg, Innovation in Materials Science and Engineering: Proceedings of ICEMIT2017, Springer Singapore **2**, 43 (2019).
[17] P. K. Todd, A. Wustrow, R. D. McAuliffe, M. J. McDermott, G. T. Tran, B. C. McBride, E. D. Boeding, Daniel O'Nolan, Chia Hao Liu, Shyam S. Dwaraknath, Karena W. Chapman, Simon J. L. Billinge, Kristin A. Persson, Ashfia Huq, Gabriel M. Veith, James R. Neilson, Inorganic Chemistry **59** (18), 13639 (2020).
[18] Y. S. Kim, W. T. Kim, D. H. Kim, Journal of Alloys and Compounds **779**, 805 (2019).
[19] A. F. Qasrawi, H. M. Zyoud, Physica Status Solidi B **257**(6), 2000089 (2020).
[20] Y. Y. Li, Y. C. Yang, T. H. Chou, Y. L. Huang, C. H. Chang, Y. L. Hsu, K. L. Lin, Journal of Electronic Materials **54**, 2211 (2025).
[21] F. Ichihara, H. Pang, T. Kako, D. W. Bahnemann, J. Ye, Nanoscale **17**, 2567 (2025).
[22] F. Zhang, B. Li, C. Li, S. Li, N. Zhang, C. Gao, K. Yang, Y. Gao, D. Zhao, X. Cui, Journal of Alloys and Compounds **991**, 174457 (2024).
[23] J. C. Rhoda, D. Pourkodee, J. P. Suchitra, M. Giruba, H. M. Albert, C. A. Gonsago, BioNanoScience **15**(1), 1 (2025).
[24] E. H. Chowdhury, M. H. Rahman, R. Jayan, M. M. Islam, Computational Materials Science **186**, 110001 (2021).
[25] M. Dresselhaus, G. Dresselhaus, S. C. Filho, AGS: Solid State Properties from Bulk to Nano, Springer-Verlag, Berlin (2017).
[26] J. Jin, K. Kang, Z. Xiao, J. Zhang, T. Y. Kim, H. S. Lee, J. Kim. Physica Status Solidi A **222**, 2400536 (2024).
[27] O. Surucu, M. Isik, N. M. Gasanly, M. Terlemezoglu, M. Parlak, Materials Letters **275**, 128080 (2020).
[28] H. H. Gullu, M. Isik, O. Surucu, N. M. Gasanly, M. Parlak, Materials Science in Semiconductor

Processing **123**, 105559 (2021).
[29] O. Madelung, Semiconductors: Data Handbook, Springer Science & Business Media, New York, 2012.
[30] A. F. Qasrawi, S. S. Atari, Optical and Quantum Electronics **57**, 605 (2025).
[31] L. C. Fan, W. S. Zhao, H. Y. Gan, L. He, Q. Liu, L. Dong, G. Wang, Sensors and Actuators A: Physical **301**, 111778 (2020).
[32] A. F. Qasrawi, B. H. Kmail, Optics and Quantum Electronics **56** (6), 978 (2024).
[33] K. Kundu, N. N. Pathak, Next Generation Wireless Communication: Advances in Optical, mm-Wave, and THz Technologies, Springer, 313 (2024).
[34] Y. Hu, Y. Wang, K. W. Chee, Smart grids and their communication systems, Ersan Kabalci, Yasin Kabalci (eds.), Springer, Singapore, 401 (2019).
[35] N. Garg, Innovation in Materials Science and Engineering, Springer, Singapore, 43 (2019).
[34] S. B. Patil, N. S. Sankeshwar, S. S. Kubakaddi, AIP Conference Proceedings **1665**(1), 110029 (2015).
[35] Z. Chen, J. Yang, X. Ding, X. Li, J. Zhang, IEEE Transactions on Electron Devices **71**(3), 1963 (2024).
[36] Y. Su, S. Cao, L. B. Shi, P. Qian, Applied Surface Science **531**, 147341 (2020).
[37] N. Collaert, New Materials and Devices Enabling 5G Applications and Beyond, Elsevier, 139 (2024).
[38] M. M. Hasan, C. Wang, N. Pala, M. Shur, Nanomaterials **14** (5), 460 (2024).
[39] S. E. Al Garni, A. F. Qasrawi, Physica E: Low-dimensional Systems and Nanostructures **105**, 162 (2019).
[40] N. M. Khusayfan, A. F. Qasrawi, S. R. Alharbi, H. K. Khanfar, T. S. Kayed, Optik **231**, 166506 (2021).
[41] B. Knebusch, L. Junemann, P. Holtje, A. Mertens, B. Ponick, 2022 24th European Conference on Power Electronics and Applications (EPE'22 ECCE Europe), IEEE, 1 (2022).
[42] E. A. Tutov, A. V. Manannikov, H. I. Al-Khafaji, V. P. Zlomanov, Technical Physics **62**, 390 (2017).
[43] S. E. Algarni, A. F. Qasrawi, N. M. Khusayfan, Applied Physics A **128** (4), 254 (2022).
[44] A. Qasrawi, H. Khanfar, Journal of the Arab American University **9**, 1 (2023).
[45] A. F. Qasrawi, T. S. Kayed, K. A. Elsayed, Physica E **86**, 124 (2017).
[46] E. Mahenge, R. Sinde, M. A. Dida, A. E. Sam, IEEE Access **12**, 43772 (2024).
[47] Y. Sun, Zh. Chen, H. Lu, Sh. Wu, Ch. Ren, Weibo Wang, Junyun Zang, Research and Progress of Solid-State Electronics **44**, 379 (2024).
[48] J. L. Jimenez-Martin, V. Gonzalez-Posadas, A. Parra-Cerrada, D. Espinosa-Adams, D. Segovia-Vargas, W. Hernandez, Sensors **24**(10), 3141 (2024).

*Corresponding author: atef.qasrawi@aaup.edu; atef.qasrawi@istinye.edu.tr